

Dispersive instabilities in Passively Mode-Locked Integrated External-Cavity Surface-Emitting Lasers

Christian Schelte^{1,2}, Denis Hessel^{1,2}, Julien Javaloyes¹, and Svetlana V. Gurevich^{1,2,3*}

¹ *Departament de Física, Universitat de les Illes Balears & Institute of Applied Computing and Community Code (IAC-3), Cra. de Valldemossa, km 7.5, E-07122 Palma de Mallorca, Spain*

² *Institute for Theoretical Physics, University of Münster, Wilhelm-Klemm-Str. 9, D-48149 Münster, Germany and*

³ *Center for Nonlinear Science (CeNoS), University of Münster, Corrensstrasse 2, D-48149 Münster, Germany*

(Dated: January 13, 2020)

We analyze the dynamics of passively mode-locked integrated external-cavity surface-emitting Lasers (MIXSELS) using a first-principle dynamical model based upon delay algebraic equations. We show that the third order dispersion stemming from the lasing micro-cavity induces a train of decaying satellites on the leading edge of the pulse. Due to the nonlinear interaction with carriers, these satellites may get amplified thereby destabilizing the mode-locked states. In the long cavity regime, the localized structures that exist below the lasing threshold are found to be deeply affected by this instability. As it originates from a global bifurcation of the saddle-node infinite period type, we explain why the pulses exhibit behaviors characteristic of excitable systems. Using the multiple time-scale and the functional mapping methods, we derive rigorously a master equation for MIXSELS in which third order dispersion is an essential ingredient. We compare the bifurcation diagram of both models and assess their good agreement.

I. INTRODUCTION

In spite of its early discovery in 1965 [1], the passive mode-locking (PML) of lasers is still a subject of intense research, not only due to its important technological applications [2, 3], but also because it involves the self-organization of a large number of laser modes that experience an out-of-equilibrium phase transition [4, 5].

Vertical external-cavity surface-emitting semiconductor lasers (VECSELs) are prominent laser sources in various industrial and scientific applications that require high output power and good beam quality [6–9]. Here, the PML phenomenon is obtained by closing the external cavity with a semiconductor saturable absorber mirror (SESAM); the intensity-dependent losses promote pulsed over continuous wave emission and lead to pulses that are typically in the picosecond range, see [10, 11] for reviews.

Among the wealth of dynamical regimes encountered in such complex photonic systems involving coupled cavities, the regular pulsating regimes have direct applications, e.g., for compact spectroscopy [12] and metrology [13]. Designs based upon the VCSEL-SESAM geometry yield output powers that evolved from 200 mW [14–16] towards 20 W [17] and, recently, transform limited pulses in the 100 fs range with peak power of 500 W [18] were obtained with repetition rate in the GHz range.

A new type of nonlinear cavity appeared in the last decade, the so-called Mode-Locked Integrated External-Cavity Surface-Emitting Lasers (MIXSEL) [19, 20] in which both the gain and the saturable absorber share the same micro-cavity. Coupling the MIXSELS to an external mirror provides for the essential optical feedback that defines the repetition rate of the pulse train.

More generally, the mode-locking of VECSELs is based upon micro-cavities operated in reflection: one or two for MIXSELS and VCSEL-SESAMs, respectively. The rich PML dynamics and the multi-pulses regimes can be controlled e.g., with time-delayed optical feedback [23, 24], coherent optical injection [25] or photonic crystal structures [26]. In addition, carrier dynamics in multi-level active materials such as quantum dots [27, 28] or sub-monolayer quantum dots [29] leads to rich behaviors. The cavity geometry also proved its relevance and peculiar pulse clusters appear in V-shaped cavities [30, 31].

While it was commonly accepted that semiconductor mode-locked lasers could not emit pulse trains at rates well below the GHz, a regime of temporal localization allowing arbitrary low repetition rates and individual pulse addressing was disclosed [21, 32–35]. This transition from PML towards addressable temporal localized structures (TLSs) could have applications for dense frequency combs generation [36] and all optical data processing [37]. To add to its technological relevance, the long cavity regime, in which the photon round-trip is longer than the semiconductor gain recovery time, is compatible with spatial confinement; stable three-dimensional light bullets were predicted in broad area micro-cavities [38–40].

Recently, a new kind of instability for the pulse trains obtained in the long cavity regime was experimentally observed in mode-locked VECSELs [22]. At its core, these unstable pulsating regimes results from the face-to-face coupling of the micro-cavities containing the gain and the saturable absorber media. Operated in reflection, the gain and absorber micro-cavities behave as dispersive Gires-Tournois interferometers (GTI) [41]. After several round-trips, the third order dispersion (TOD) induced by the micro-cavities give rise to serrated wave forms that consists in a decaying sequence of satellites accumulating in front of the leading edge of the pulse.

* gurevics@uni-muenster.de

It was shown that these satellites may become unstable leading to a low frequency modulation of the pulse envelope on a slow time scale, typically on the order of hundreds of round-trips. Understanding this regime is of paramount importance in order to avoid time and amplitude jitter and spectral broadening of the lines forming the frequency comb of the PML regimes.

In this manuscript, we predict that such dispersive instabilities may also occur in MIXSELs. While MIXSELs micro-cavities contain both the gain and the saturable absorption, they are also operated in reflection and it stands to reason that they shall exhibit the same dispersive behavior characteristics of GTIs. Finally, due to its simpler geometry, the MIXSEL proves to be a particularly instructive minimal model for our analysis.

We present in Sec. II a first principle model for the MIXSEL. Following the method of [42], it consists in solving analytically the field propagation in the linear sections of the micro-cavity, while considering the gain and absorber sections as nonlinear boundary conditions. The boundary conditions for the field at the micro-cavity/air interface together with the optical feedback from the external mirror impose the structure of the model as time-delayed algebraic equations (DAEs). We propose to conduct what we believe to be the first bifurcation analysis of such DAEs model in Photonics. We demonstrate in Sec. III, how a series of decaying satellites on the leading edge of the pulse causes an instability of the pulse train and how a global bifurcation with features of excitability as well as more intricate oscillating dynamics can appear in Sec. IV and V, respectively. Using the rigorous formalism of the multiple time-scale [43] as well as the newly developed functional mapping method [40], we complement our analysis in Sec. VI with the derivation of a master equation governing the slow pulse evolution over the round-trip time scale, similar to the so-called Haus master equation [10], and that takes the form of a generalized complex Ginzburg-Landau partial differential equation (PDE). The latter allows to identify why TOD has such an important effect in the dynamics of MIXSELs. Finally, using modern continuation techniques [44], we compare the results of the PDE with that of the DAE model and find in which conditions a good agreement can be obtained.

II. MODEL SYSTEM

The schematic setup of a MIXSEL system is depicted in Fig. 1. The gain and the absorber media are enclosed into micro-cavities whose length is of the order of the lasing wavelength. The two mirrors of the micro-cavity provide additional degrees of freedom for controlling the light-matter interaction. The interaction strength with the active medium—that is only a few tens of nanometers long—can be dramatically increased, as the expense of the available bandwidth, by using high-Q cavities. Similarly, the effective saturation of the active material

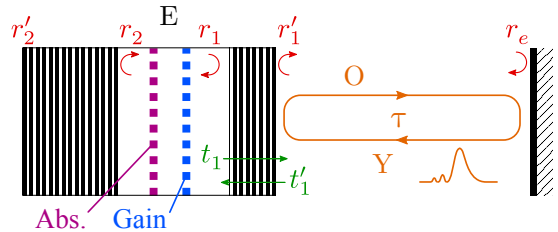


Figure 1. (color online) A schematic of the MIXSEL configuration, where both gain (blue) and saturable absorption (magenta) are contained in the same microcavity. E denotes the field amplitude in the active region. The output and injection fields in the external cavity are represented by O and Y , respectively. The external cavity round-trip time is τ .

can be increased (or decreased) by using resonant or anti-resonant cavity designs, respectively. Because of the vast scale separation between the external cavity length and that of the micro-cavity, the natural framework for our analysis is that of time-delayed systems. The latter appear not only as natural modeling approaches for PML [42, 45] but in many branches of physics. Delayed systems have strong links with spatially extended systems such as the Ginzburg-Landau equation [46, 47] and lead to rich dynamical behaviors [48–52], see [53] for a review.

We consider the case of a resonant cavity and we denote by E the micro-cavity field over an antinode and Y the field in the external cavity. The output field is denoted by O , τ is the external cavity round trip time, whereas $r_{1,2}$ are the top and bottom Distributed Bragg Reflector (DBR) reflectivities, t_1 is the transmission coefficient of the top DBR and r_e is the external mirror reflectivity. We follow the approach of [42] that consists in solving the field propagation in the linear sections of the micro-cavity. That way one obtains a dynamical model linking the two fields E and Y . Their coupling is achieved considering the transmission and reflection coefficients of the top DBR. After normalization, one obtains the rate equations for the field E , the gain N_1 and absorber N_2 population inversions as

$$\dot{E} = [(1 - i\alpha_1) N_1 + (1 - i\alpha_2) N_2 - 1] E + hY, \quad (1)$$

$$\dot{N}_1 = \gamma_1 (J_1 - N_1) - |E|^2 N_1, \quad (2)$$

$$\dot{N}_2 = \gamma_2 (J_2 - N_2) - s |E|^2 N_2, \quad (3)$$

$$Y = O(t - \tau) = \eta [E(t - \tau) - Y(t - \tau)]. \quad (4)$$

We scaled Eqs. (1-4) by the photon lifetime in the micro-cavity τ_p , and α_1 and α_2 are the linewidth enhancement factors of the gain and absorption, respectively. We set the bias and the recovery time in the gain as (J_1, γ_1) and in the absorber section as (J_2, γ_2) , respectively. The ratio of the gain and absorber saturation intensities is s .

The cavity enhancement due to the high reflectivity mirrors can be scaled out, making that E and Y are of the same order of magnitude. This scaling has the additional advantage of simplifying the input-output relation of the micro-cavity; using Stokes relations, we find that

it reads $O = E - Y$. The minus sign represents the π phase shift of the incoming field Y upon reflection from the top DBR. After a round-trip in the external cavity of duration τ , the output field $O(t - \tau)$ is re-injected with an attenuation factor $\eta = r_e \exp(\omega_0 \tau)$, with $\omega_0 \tau$ the propagation phase, defining ω_0 as the carrier frequency of the field. The coupling between E and Y is given in Eq. (4) by a delayed algebraic equation (DAE), that takes into account the multiple reflections in the external cavity. In the limit of a very low external mirror reflectivity $\eta \ll 1$, one would truncate the infinite hierarchy generated by Eq. (4) to obtain $Y = \eta E(t - \tau) + \mathcal{O}(\eta^2)$ leading to the so-called Lang-Kobayashi model [54]. Yet, for mode-locked configurations $\eta = \mathcal{O}(1)$ and the multiple reflections in the external cavity must be taken into account. Instead of considering an infinite number of delayed terms in Eq. (1) with values $\tau, 2\tau, \dots, n\tau$, the DAE given by Eq. (4) allows for an elegant representation of the strongly coupled cavity dynamics without needing an *a priori* truncation.

The coupling efficiency of the external field Y into the micro-cavity is given by the parameter $h = (1 + |r_2|)(1 - |r_1|)/(1 - |r_1 r_2|)$. There exist three instructive limit cases for the coupling parameter h that correspond to certain types of devices: A non-transmitting top DBR $|r_1| = 1$ yields $h = 0$, making the cavity equivalent to a perfect (linear) mirror. Equal reflectivities for both DBRs $|r_1| = |r_2|$ yield $h = 1$ and correspond to a symmetric Fabry-Perot cavity. Finally, a fully reflecting bottom DBR $|r_2| = 1$ yields $h = 2$, which corresponds to the GTI case [41]. Gires-Tournois interferometers are known for inducing controllable second order dispersion and they are used as optical pulse shaping elements. Resonant photons transmitted into the micro-cavity will remain on average for the photon lifetime. When transmitted back into the external cavity they will have collected a phase difference with respect to the off-resonance photons that are directly reflected upon the top DBR. Note that this phase shift is a function of the detuning of the photons with respect to the closest micro-cavity mode. The recombination of various wavelength in the external cavity leads to dispersion. This process is fully captured by Eq. (1-4). Second order dispersion is typically the dominating effect and its amount is tunable by choosing the detuning. Using red or blue detuning one can achieve either normal or anomalous dispersion while around resonance TOD becomes the leading term as the second order contribution vanishes and switches sign. Gires-Tournois interferometers are designed to conserve the photon number using high reflective bottom mirrors and therefore yield purely dispersive spectrum in models such as given by Eqs. (1-4), see [22] for more details.

In order to achieve directional emission and low losses the bottom DBRs of VCSELs are optimized towards $|r_2| \rightarrow 1$, i.e., they are well approximated by the GTI regime and $h \rightarrow 2$. We set the photon lifetime as $\tau_p = 3$ ps which corresponds to a Full Width at Half Max-

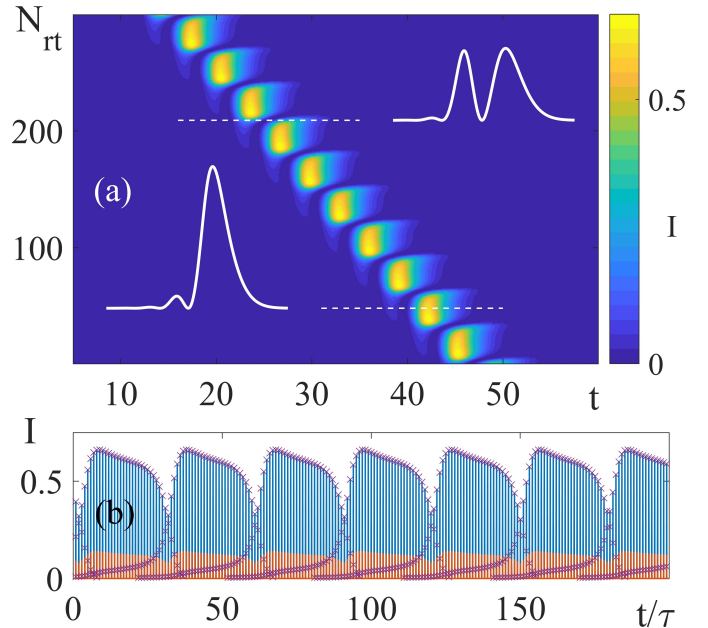


Figure 2. (color online) Pseudo-space-time diagram (a) and time trace (b) for the pulse train in the unstable satellite regime obtained from DNSs of Eqs. (1-4). The pulse intensity for E (blue) and Y (orange) fields is shown. The purple crosses at the intensity peaks illustrate the creation-annihilation cycle. For sufficiently large gain the largest satellite is amplified, eventually replacing its parent pulse. Parameters are $(J_1, \alpha_1, \alpha_2) = (0.65, 0, 0)$.

imum (FWHM) of $(\pi\tau_p)^{-1} = 106$ GHz. The gain and absorber lifetimes are 1 ns and 30 ps, respectively, while we set the round-trip time in the cavity to 3 ns, hence $(\gamma_1, \gamma_2, \tau) = (0.003, 0.1, 1000)$. If not stated otherwise, the other parameters are $(J_2, \eta, s, h) = (-0.5, 0.7, 10, 2)$.

III. SATELLITE INSTABILITY

Due to TOD from the GTI-like micro-cavity pulses can have a series of decaying satellites on the leading edge that was found to cause an instability of the pulse train [22]. Without linewidth enhancement factors $\alpha_1 = \alpha_2 = 0$ the satellites are most clearly developed because of the absence of chirp and their instability can be better understood starting from this situation. In a real semiconductor medium the change in carrier density along the pulse profile causes a varying detuning with respect to the micro-cavity resonance due to the alpha factors. The resulting mixture between chirp and dispersion creates a more involved dynamics that will be discussed later in this manuscript.

We operated in the regime of localization where the pulses are temporal localized states that appear below the lasing threshold bias defined as J_1^{th} . As detailed in [32], the TLSs appear via a saddle-node bifurcation of limit cycles. Sufficiently close to the lasing threshold,

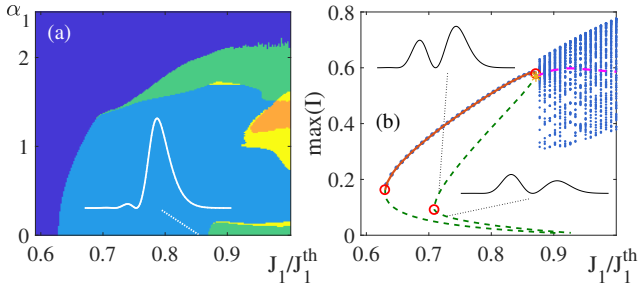


Figure 3. (color online) (a) Bifurcation diagram in the (J_1, α_1) -plane obtained with DNSs of Eqs. (1-4) for $\alpha_2 = 0$. The off, stable pulsating, and quasi-periodic pulsating regimes are shown in dark blue, light blue and green, respectively. Bistable regions are orange and yellow for stable and oscillating solutions. Pure satellite instability is observed for low α_1 whereas trailing edge AH instability for high α_1 values. Both can mix forming the region around $\alpha_1 \approx 1$ close to threshold that is bistable with stable pulses. (b) Branch of a single pulse solution showing $\max(I)$ as a function of the scaled gain bias J_1 , superposing results from DNS (blue points) and path-continuation for $\alpha_1 = 0$. Orange solid line shows the stable part of the branch which becomes unstable (green dashed line) in a fold of the limit cycle (red circles), i.e., the satellite instability does not stem from secondary AH bifurcation. After the fold on the unstable branch there is a supercritical pitchfork bifurcation (yellow star) that gives birth to another unstable branch (dashed magenta).

the main pulses and therefore their parasitic satellites become large enough to bleach the absorber and open the net gain window prematurely. As a consequence, they grow exponentially from one round-trip towards the next while the parent pulse meets an increasingly depleted gain carrier density and eventually dies out. It is replaced by its satellite in front, resulting in forward leaping motion that can best be seen in a pseudo-space-time representation which is shown in Fig. 2(a) where N_{rt} is the number of round-trips. The corresponding temporal trace obtained from direct numerical simulations (DNSs) of Eqs. (1-4) is depicted in Fig. 2(b). It demonstrates how this cycle of creation and annihilation leads to a low frequency modulation of the pulse train (see the purple crosses).

A full bifurcation analysis of the DAE system (1-4) is out of the scope of the current manuscript. The main reason being that the stability analysis of periodic solutions of DAEs is not possible at the moment, even using the most advanced continuation softwares such as DDE-BIFTOOL [55]. Yet, we show in Fig. 3(a) a numerical two parameter bifurcation diagram in the (J_1, α_1) plane for the single pulse solution. The stable region and off solution are depicted in light and dark blue, respectively, in Fig. 3(a). For high values of the linewidth enhancement factor of the gain α_1 , a quasi-periodic instability due to self-phase modulation is found, similar to that discussed in [56]. This instability was found to be a local secondary Andronov-Hopf (AH) bifurcation. In addition to these

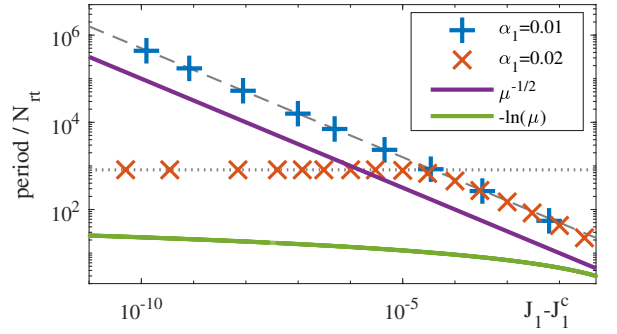


Figure 4. (color online) The dependence of the period length on the distance to the bifurcation point J_1^c . The crosses denote the period obtained from DNSs of Eqs. (1-4) for $\alpha_1 = 0.01$ (blue) and $\alpha_1 = 0.02$ (orange). The straight lines correspond to the theoretically predicted scaling behavior for a homoclinic (green) as well as for a SNIPER (purple) bifurcation.

regimes, that exists in the generic mode-locked ring laser model of [45], a new instability induced by TOD is found for low values of α_1 . It corresponds to the regime depicted in Fig. 2. Both unstable regions are depicted in green. In addition, around $\alpha_1 \approx 1$, there exists a bistable region close to threshold between a stable PML regime with higher intensity pulses and low frequency modulated PML; this latter quasi-periodic dynamics has the characteristics of both instabilities found for low and large α_1 ; it is discussed in more detail in Section V. The bistable region is depicted in orange where stable and modulated pulses are stable and yellow where only one solution is stable. Note that parts along the borders of the pure instabilities are also bistable with a regular PML solution with smaller pulses.

We show in Fig. 3(b) the branch for the single TLS solution obtained using DDE-BIFTOOL. At $\alpha_1 = 0$, the solution branch folds three times with the second fold at a critical value of the current $J_1^c \sim 0.86 J_1^{\text{th}}$ that coincides with the onset of the satellite instability. The results from the corresponding DNSs are superposed (blue points), indicating the all the values of the pulse maxima integrated over many round-trips. Shortly after the second fold, a second unstable branch (dashed magenta) appears in a pitchfork bifurcation. Above J_1^c , no stable single pulse solution branch exists and one observes the low frequency periodic dynamics discussed in Fig. 2.

It has to be noted that for $\alpha_1 \ll 1$ this instability does not stem from a local Andronov-Hopf bifurcation but from a global bifurcation. The limit cycle is born with infinite period at the second fold of the TLS branch in Fig. 3(b). The period scaling is presented in Fig. 4 where we show the period evolution for two exemplary values of α_1 (blue and orange crosses) and the characteristic scalings for saddle-node infinite period ($\mu^{-1/2}$) and homoclinic ($\ln \mu^{-1}$) bifurcations as a function of the distance to the bifurcation point J_1^c . The results reveal that for small values of α_1 the satellite instability can be iden-

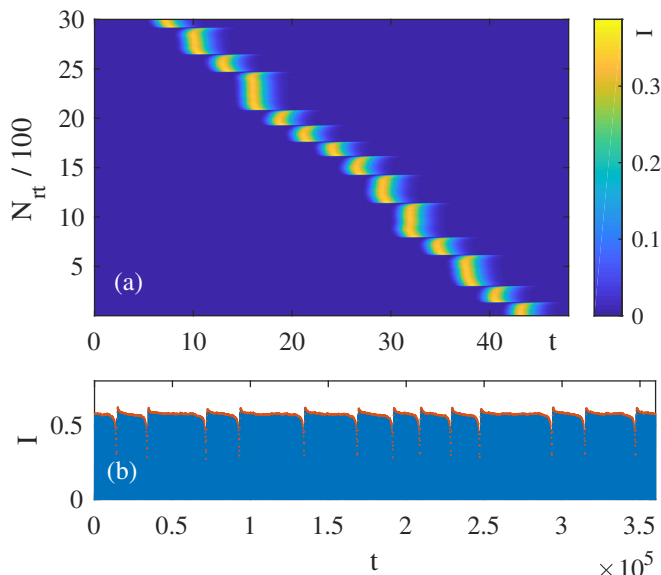


Figure 5. (color online) (a) Pseudo-space-time diagram for a single pulse obtained in DNSs of (1-4) showing excitable behavior. Close to the SNIPER bifurcation point, satellites grow slowly as they are barely able to bleach the absorber sufficiently. High noise has a very strong influence on the blow-up time in this situation. (b) Corresponding time trace of the pulse intensity with the pulse maxima highlighted in orange.

tified to be of the saddle-node infinite period (SNIPER) type. However, for increasing α_1 the SNIPER bifurcation changes into a local AH bifurcation (cf. the scaling for $\alpha_1 = 0.02$).

IV. EXCITABILITY

Under the influence of noise the satellite instability exhibits dynamical behavior characteristics of excitable systems. To trigger the replacement of the parent pulse a satellite must have sufficient intensity to bleach the absorber and open an early net-gain window. Close, yet below, to the critical energy, noise can help or hinder the satellite emergence by adding or subtracting some energy, respectively. As a result, the period of the pulse eruptions can become highly irregular and we present in Fig. 5 an exemplary pseudo-space-time diagram for a single pulse (a) and the corresponding time trace (b) in the excitable regime. By all accounts, this is certainly in its irregular form that such a regime is most likely going to appear in an experimental situation, where noise is unavoidable.

In Fig. 6 we show the statistical properties of the satellite instability under the influence of gaussian noise with a standard deviation of σ_{noise} for varying distances of the gain bias J_1 from the critical value J_1^c corresponding to the onset of the SNIPER bifurcation. Panel (a) shows the mean value and panel (b) the standard deviation of the period of the satellite eruptions. At each point of the di-

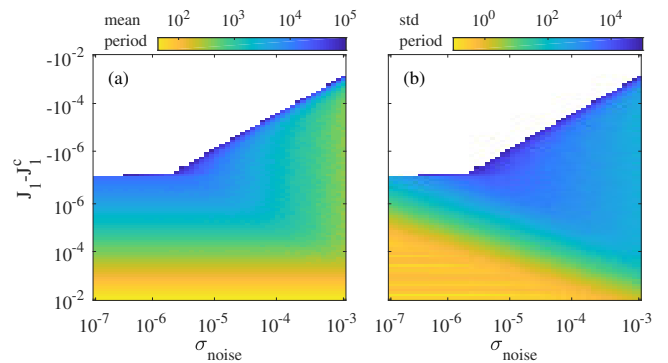


Figure 6. (color online) The dependence of the mean value (a) and standard deviation (b) of the period of the satellite instability as a function of the noise parameter σ_{noise} and the distance of J_1 to the bifurcation point J_1^c . Parameters are $(\alpha_1, \alpha_2) = (0, 0)$.

agrams hundred of consecutive eruptions were analyzed. To make such calculations feasible, the simulations were performed in the long delay limit using the functional mapping approach [40]. One can see how noise enables eruptions below the critical pump rate. The stronger the noise the less gain bias is necessary for this. The cutoff visible in the data is arbitrary, as the necessary integration times grows very fast and becomes a limiting factor to the feasibility of DNSs. Statistically, eruptions can happen anywhere, albeit very rarely depending on the parameters. For increasingly strong noise the observed average period decreases and depends little on the actual gain bias. Similarly, for strong pumping the noise hardly changes the mean period. The standard deviation of the eruptions is very large at the onset below critical pumping due to noise. Here the eruptions are rare and the excitability is most visible. Otherwise the variance decreases with both increasing gain bias and decreasing noise level.

V. COMBINED INSTABILITIES

With realistic linewidth enhancement factors for semiconductor media the satellite and self-phase modulation instabilities combine to form a dynamics of the kind presented in [22]. By performing parameter scans as a function of various parameters we were able to deduce some rules of thumb for this satellite instability. Generally, the pulse-width is proportional to the photon lifetime and can be written as $\tau_p = \kappa^{-1} f(\dots)$ with $f(\dots)$ a function that depends on all the other parameters of the PML setup. Optimizing PML consists in finding the parameter combination for which the function f is the smallest. Since the temporal separation between the main pulse and its first satellite is fixed by the cavity photon lifetime, it is *in these optimal cases* where, as depicted in Fig. 2, that the satellites become better resolved from the main pulse and where they are prone to become un-

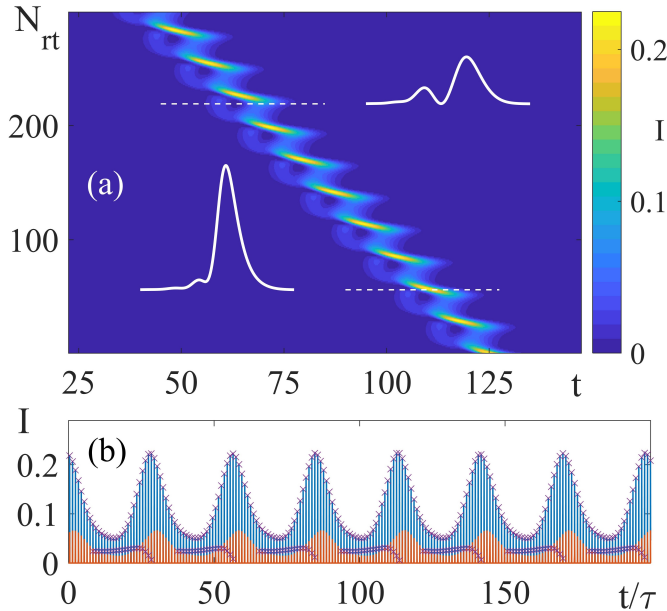


Figure 7. (color online) Pseudo-space-time diagram (a) and corresponding time trace (b) for the single pulse train in the satellite unstable regime. The pulse intensity for E (blue) and Y (orange) fields are shown. With realistic values of the linewidth enhancement factors the dynamics is more involved due to the chirp that induces pulse broadening. Here, instead of dying out completely the parent pulse merges with its growing satellite. Parameters are $(J_1, \alpha_1, \alpha_2) = (0.65, 2.1, 0.5)$.

stable. Hence, the satellite instability can be obtained by tuning any parameter leading to the optimal PML and shortest pulse-width, making this instability an essential limitation in the optimization procedure to find the narrowest pulses. For instance, increasing the saturation s or even the linewidth enhancement factor of the absorber α_2 , if it compensates for the chirp induced in the gain section, can adversely narrow the pulse which destabilizes the PML regime. In “bad conditions” the pulse and its satellites are smeared out into a globally broader pulse that is stable. Note that in the VCSEL-SESAM setup studied in [22] the detuning between the two micro-cavities is an additional factor leading to further complexity since second order dispersion also plays a role. Finally, we show in Fig. 7 how the satellite instability evolves for more realistic situations setting $\alpha_1 = 2.1$ and $\alpha_2 = 0.5$. We note that, in addition, this regime can be bistable with the stable pulsating solution, as shown in the orange region in Fig. 3(a).

VI. THE DISPERSIVE MASTER EQUATION

Bifurcation analysis does not always allow for an intuitive interpretation of the dynamics. In addition, even if the time delayed equations Eqs. (1-4) contain a lot of the physics of PML, their form remains complicated. For instance, their dispersive features do not appear so obvi-

ous. We derive in this section a PDE for the field amplitude E that approximates the dynamics of the full DADE model (1-4). In the PDE representation, the field depends on a slow and a fast time, i.e. $E \equiv E(\xi, z)$. Here, the slow time (ξ) represents the evolution of the field profile from one round-trip to the next while the “spatial variable” (z) describes the fast evolution of the pulse within the round-trip. While this approach has been used in several time-delayed systems, see e.g., [52, 53] for a review, such PDE models are usually termed Haus master equations in the framework of mode-locking, see [10] for a review.

In the case of high frequency PML dynamics, i.e. the regimes in which the cavity round-trip is much shorter than the gain recovery time, a PDE approximating the dynamics of a ring cavity model based upon delay differential equations [45] was proposed in [57]. The multiple time-scales analysis method was used and the scaling of parameters consisted in assuming low losses, low gain, and weak spectral filtering. In the model of [45], these three physical effects are controlled by three independent parameters. In the multiple time-scales approach one finds, at the lowest order, a periodic solution, e.g., a pulse evolving over the fast time scale (z) that circulates in the cavity without deformation. At third order in the expansion scheme, a solvability condition allows finding that the dynamics on the slow time scale (ξ) is governed by the weak effects of gain, loss and spectral filtering. In a PDE representation, the gain filtering in the model of [45] takes the form of a diffusion over the fast time, i.e. a term $d_2 \partial_z^2 E$ with $d_2 > 0$. While the smallness of gain, losses and filtering can be, in some situations, debatable, the advantage of the approach presented in [57] is the uniform accuracy of the PDE representation that was not, e.g., limited to the vicinity of the lasing threshold. For instance, no *a priori* conditions over the magnitude of the field were necessary.

It is interesting—and surprising—to notice that the aforementioned approach fails if one tries to export it to the case of the DADE model (1-4); the resulting PDE obtained similarly as a third order solvability condition does possess gain and losses, yet it is devoid of spectral filtering ($d_2 = 0$) which leads to singular dynamics and unphysical pulse collapse. The physical reason that underlies this mathematical phenomenon is that the filtering of the micro-cavity is not in our modeling approach independent from gain and losses. It is the actual level of the population inversion in the micro-cavity that defines the breadth and hence the curvature of the resonance. This effect is particularly pronounced in the Gires-Tournois regime (i.e., $h = 2$), where the empty cavity reflectivity is unity, which corresponds to no curvature at all and $d_2 = 0$. That is, positive (resp. negative) curvature induces diffusion (resp. anti-diffusion). Generally, the average gain experienced by the pulse must be positive to compensate for the cavity losses incurred by the mirror reflectivity η .

A proper analysis of the model given by Eqs. (1-4)

shall result in a PDE whose diffusion term d_2 depends on other parameters such as the cavity losses. This discussion materializes by taking as the expansion point the cavity at the lasing threshold instead of the empty cavity, as done in [57]. At the lasing threshold, the unsaturated gain and losses exactly compensate. This modification will allow to obtain the filtering induced by the cavity at threshold, instead of that of the empty cavity leading to $d_2 = 0$. The drawback of our approach is that we have to assume the pulse to be not too intense and treat the nonlinear effects perturbatively, limiting our analysis to the vicinity of the lasing threshold.

We start by normalizing time by the cavity round-trip τ time as $\sigma = t/\tau$ and define a smallness parameter $\varepsilon = 1/\tau$. As we operate in the long cavity limit, the carriers are not independent functions of time that can lead to resonant terms and solvability conditions. Instead, the carrier evolutions depend uniquely on the initial conditions at the beginning of the round-trip, which in the long cavity limit is the equilibrium value, and on the amplitude of the field, i.e., $N_j = N_j(J_j, E)$. Hence, we can concentrate solely on the field dynamics that reads

$$\varepsilon \frac{dE}{d\sigma} = [(1 - i\alpha_1)N_1 + (1 - i\alpha_2)N_2 - 1]E + hY, \quad (5)$$

$$Y(\sigma) = \eta[E(\sigma - 1) - Y(\sigma - 1)]. \quad (6)$$

We assume a small deviation of the gain and absorber with respect to their equilibrium values that we scale as

$$N_j = J_j + \varepsilon^3 n_j \quad (7)$$

with $j \in [1, 2]$. We also assume η to be real as the feedback case is irrelevant in the long cavity regime. Defining the Fourier transform of the field profiles at the n -th round-trip as (E_n, Y_n) and using that $\frac{d}{d\sigma} \rightarrow -i\omega$ we ob-

tain

$$(1 - G_t - i\varepsilon\omega)E_n = hY_n + \varepsilon^3 \sum_{j=1}^2 (1 - i\alpha_j)(n_j E)_n,$$

where we used the shorthand for the total complex gain $G_t = (1 - i\alpha_1)J_1 + (1 - i\alpha_2)J_2$. Noticing that the DAE for $Y(\sigma)$ in Fourier space reads

$$Y_n + \eta Y_{n-1} = \eta E_{n-1} \quad (8)$$

and, by making a linear combination of E_n and ηE_{n-1} , we get after simplification a *functional mapping*

$$E_n = \eta \frac{h - 1 + G_t + i\varepsilon\omega}{1 - G_t - i\varepsilon\omega} E_{n-1} + \varepsilon^3 \frac{1}{1 - G_t - i\varepsilon\omega} \sum_{j=1}^2 (1 - i\alpha_j) [(n_j E)_n + \eta (n_j E)_{n-1}]. \quad (9)$$

Now we impose the value of G_t to be a convenient expansion point and we set the threshold condition over the linear multiplier μ

$$\mu = \eta \frac{h - 1 + G_t + i\varepsilon\omega}{1 - G_t - i\varepsilon\omega} = 1, \quad (10)$$

which allows finding the lasing frequency shift at threshold as $\varepsilon\omega_t = \alpha_1 J_1 + \alpha_2 J_2$. This leaves us with a real equation for the amplification factor

$$\eta \frac{h - 1 + N_t}{1 - N_t} = 1, \quad (11)$$

where we defined $N_t = J_1 + J_2$. The last relation implies that the threshold is defined by

$$N_t = J_1 + J_2 = 1 - \frac{h\eta}{1 + \eta}. \quad (12)$$

We can now express the field multiplier μ from one round-trip towards the next as

$$\mu(\omega, N_t) = \eta \frac{h - 1 + N_t + i\varepsilon(\omega - \omega_t)}{1 - N_t - i\varepsilon(\omega - \omega_t)} \quad (13)$$

and the functional mapping given by Eq. 9 reads

$$E_n = \eta \frac{h - 1 + N_t + i\varepsilon(\omega - \omega_t)}{1 - N_t - i\varepsilon(\omega - \omega_t)} E_{n-1} + \varepsilon^3 \frac{1}{1 - N_t - i\varepsilon(\omega - \omega_t)} \sum_{j=1}^2 (1 - i\alpha_j) [(n_j E)_n + \eta (n_j E)_{n-1}]. \quad (14)$$

One only needs Eq. 14 to be accurate up to third order in ε in order to obtain the proper expression of the diffusion, TOD and nonlinear terms. As such, we can simplify the last term of Eq. 14 by replacing the value of E_n at the lowest order, i.e., we can set

$$E_n = \eta \frac{h - 1 + N_t}{1 - N_t} E_{n-1} + \mathcal{O}(\varepsilon) = E_{n-1} + \mathcal{O}(\varepsilon), \quad (15)$$

where we used the threshold definition given by Eq. 12. Using that $E_n = E_{n-1}$ in the nonlinear term of 14, replacing the expression of the threshold and noticing that all the frequencies are relative to that of the lasing thresh-

old, so that one can set $\tilde{\omega} = \omega - \omega_t$, yields the expression

$$E_n = \eta \frac{h-1+N_t+i\varepsilon\tilde{\omega}}{1-N_t-i\varepsilon\tilde{\omega}} E_{n-1} + \varepsilon^3 \frac{(1+\eta)^2}{h\eta} \sum_{j=1}^2 (1-i\alpha_j) (n_j E)_{n-1} + \mathcal{O}(\varepsilon^4). \quad (16)$$

Now let us assume there exists a PDE for the field $E(\xi, z)$ with ξ and z the slow and fast times, respectively. In Fourier space for the variable z , one obtains

$$\partial_\xi E = \mathcal{L}(\tilde{\omega}) E + \varepsilon^3 \mathcal{N}(\xi, \tilde{\omega}). \quad (17)$$

The form of Eq. 17 consists naturally of a linear operator $\mathcal{L}(\tilde{\omega})$ that should correspond to the linear multiplier of the mapping in Eq. 16, while $\mathcal{N}(\sigma, \tilde{\omega})$ accounts for nonlinear gain and absorber effects. We assume that $\mathcal{L}(\tilde{\omega})$ is small, i.e., $\mathcal{L}(\omega) \sim 0 + \mathcal{O}(\varepsilon)$. Such a scaling is consistent with the definition of the lasing threshold and will be checked a posteriori. Integrating *exactly* Eq. 17 over a round-trip yields

$$E_n = e^{\mathcal{L}} E_{n-1} + \varepsilon^3 \int_{n-1}^n e^{(n-\xi)\mathcal{L}} \mathcal{N}(\xi, \tilde{\omega}) d\xi. \quad (18)$$

Because the integral term in Eq. 18 is already at third order in ε , we can approximate $e^{(n-\xi)\mathcal{L}} = 1 + \mathcal{O}(\varepsilon)$ and evaluate the nonlinear operator using the Euler explicit method. Indeed, since \mathcal{N} depends on the field, the error in the integration will be proportional to the slow evolution of the field from one round-trip towards the next, i.e., $\partial_\xi \mathcal{N} \sim \partial_\xi E \sim \mathcal{O}(\varepsilon)$. That is, we find

$$E_n = e^{\mathcal{L}} E_{n-1} + \varepsilon^3 \mathcal{N}(n-1, \tilde{\omega}) + \mathcal{O}(\varepsilon^4). \quad (19)$$

Comparing Eq. 16 and Eq. 19 we deduce that

$$\mathcal{L} = \ln \left(\eta \frac{h-1+N_t+i\varepsilon\tilde{\omega}}{1-N_t-i\varepsilon\tilde{\omega}} \right). \quad (20)$$

whereas the equations for the carriers take the form

$$\frac{\partial N_1}{\partial z} = \gamma_1 (J_1 - N_1) - |E|^2 N_1, \quad (29)$$

$$\frac{\partial N_2}{\partial z} = \gamma_2 (J_2 - N_2) - s|E|^2 N_2. \quad (30)$$

Using Eq. 12 the last expression can be simplified as

$$\mathcal{L} = \ln \left(\frac{1 + i\varepsilon\eta \frac{1+\eta}{h\eta} \tilde{\omega}}{1 - i\varepsilon \frac{1+\eta}{h\eta} \tilde{\omega}} \right). \quad (21)$$

We can verify easily that $\mathcal{L} = \mathcal{O}(\varepsilon)$ which allows to check a posteriori our approximation regarding the order of the operator \mathcal{L} . One can also expand Eq. 21 in $\tilde{\omega}$ up to third order will yields the drift, diffusion and TOD coefficients d_1, d_2 and d_3 as

$$\mathcal{L} = d_1 (-i\varepsilon\tilde{\omega}) + d_2 (-\varepsilon^2\tilde{\omega}^2) + d_3 (i\varepsilon^3\tilde{\omega}^3) + \mathcal{O}(\varepsilon^4) \quad (22)$$

with

$$d_1 = -\frac{(\eta+1)^2}{h\eta}, \quad (23)$$

$$d_2 = \frac{1-\eta^2}{2} \left(\frac{\eta+1}{h\eta} \right)^2, \quad (24)$$

$$d_3 = -\frac{\eta^3+1}{3} \left(\frac{\eta+1}{h\eta} \right)^3. \quad (25)$$

The values of the coefficient d_j is particularly instructive and, in particular, how they deviate from the expression one can find easily in the case of an empty Gires-Tournois micro-cavity coupled to an external mirror: $(d_1, d_2, d_3) = (-2, 0, -2/3)$. Here, we notice that although d_1 and d_3 are somehow modified by the value of the cavity losses, the value of d_2 is not vanishing. In the good cavity limit $\eta \rightarrow 1$, we have $d_2 \sim 1 - \eta \rightarrow 0$, which explains why TOD is important as it becomes the leading order term.

Further, we identify the nonlinear operator \mathcal{N} as

$$\mathcal{N}(n-1, \tilde{\omega}) = \frac{(1+\eta)^2}{h\eta} \sum_{j=1}^2 (1-i\alpha_j) (n_j E)_{n-1} \quad (26)$$

Finally, reverting Eq. 17 to direct space using that $-i\varepsilon\tilde{\omega} \rightarrow \partial_z$, the sought PDE for the field E reads

$$\begin{aligned} \partial_\xi E &= (d_1 \partial_z + d_2 \partial_z^2 + d_3 \partial_z^3) E \\ &+ \frac{(1+\eta)^2}{h\eta} \sum_{j=1}^2 (1-i\alpha_j) (N_j - J_j) E. \end{aligned} \quad (27)$$

By using the definition of the lasing threshold and of the carrier frequency, we find that the dispersive master equation for the field E in the long cavity limit reads

$$\partial_\xi E = (d_1 \partial_z + d_2 \partial_z^2 + d_3 \partial_z^3) E + \frac{(1+\eta)^2}{h\eta} \left\{ (1-i\alpha_1) N_1 + (1-i\alpha_2) N_2 - 1 + \frac{h\eta}{1+\eta} - i\omega_t \right\} E, \quad (28)$$

Note that the rotation term $i\omega_t$ in Eq.(28) is immaterial and can be removed by setting $\tilde{E}(\xi, z) = E(\xi, z) \exp(i\omega_t \xi)$.

First we studied the PDE model (28)-(30) numerically

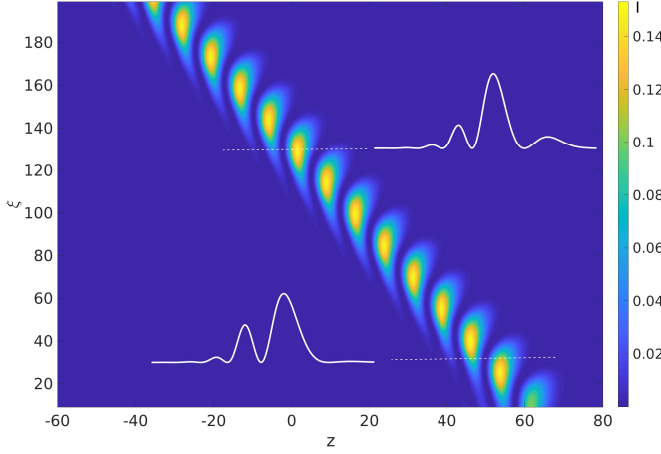


Figure 8. (color online) Space-time diagram of the satellite instability found in the DNS of the master PDE (28-30). The pulse intensity $I = |E|^2$ is shown. Parameters are $(J_1, J_2, \alpha_1, \alpha_2, \eta, s) = (0.119, -0.1, 0, 0, 0.9, 15)$.

to demonstrate the existence of the satellite instability in the parameter space and the resulting space-time diagram obtained for zero linewidth enhancement factors $\alpha_1 = \alpha_2 = 0$ is shown in Fig. 8. Again, we observe the clean cut satellite instability in this parameter range, but also that our PDE approximates very well the dynamics of the underlying time delayed model.

To compare the PDE (28)-(30) with the DAE (1-4) in detail we performed bifurcation analysis of the PDE by using pseudo-arclength continuation methods within the pde2path framework [44]. To this aim, first we seek for the steady localized pulse solutions of Eqs. (28)-(30) that can be found by setting $E(z, \xi) = A(z - v\xi)e^{-i\varpi\xi}$ leading to the following equation for the stationary field A

$$0 = v \frac{\partial A}{\partial z} + d_2 \frac{\partial^2 A}{\partial z^2} + d_3 \frac{\partial^3 A}{\partial z^3} + i\varpi A + \frac{(1 + \eta)^2}{h\eta} \left((1 - i\alpha)N_1 + (1 - i\beta)N_2 - 1 + \frac{h\eta}{1 + \eta} \right) A. \quad (31)$$

Note that both the spectral parameter ϖ and the drift velocity v become free parameters that can be found by imposing additional auxiliary integral conditions. In addition we set the following boundary conditions for the domain $z \in [0, L]$

$$\begin{aligned} \frac{\partial A}{\partial z} \Big|_{z=0, L} &= 0, \\ N_1 \Big|_{z=0} &= J_1, \quad -\frac{\partial N_1}{\partial z} \Big|_{z=L} + \gamma_1 (J_1 - N_1 \Big|_{z=L}) = 0, \\ N_2 \Big|_{z=0} &= J_2, \quad -\frac{\partial N_2}{\partial z} \Big|_{z=L} + \gamma_2 (J_2 - N_2 \Big|_{z=L}) = 0. \end{aligned}$$

Now we can follow the TLS of the PDE (28)-(30) in parameter space and in Fig. 9 we present two branches of TLSs for different values of the linewidth enhancement factors. Panel (a) shows the intensity of the TLS

as a function of the normalized pump rate for the case of $\alpha_1 = \alpha_2 = 0$. Like in the DAE case (cf. Fig. 3), one can see that the branch folds three times (points \mathbf{F}_i) when continuing in the pump rate J_1 and the second fold \mathbf{F}_2 is responsible for the SNIPER bifurcation after the first leading satellite becoming sufficiently large to saturate the absorber (cf. Fig. 8). Note that an additional unstable branch connects to the main one in a branching point \mathbf{BP} . Panel (b) shows the same gain interval for non-vanishing linewidth enhancement factors $\alpha_1 = 1.5$ and $\alpha_2 = 0.5$. Here, the branch continues without the additional folds \mathbf{F}_2 and \mathbf{F}_3 and only becomes Andronov-Hopf unstable at large gain value. Indeed, the second fold and the branching point have merged while the part of the branch with the third fold has detached, giving a qualitatively different scenario. The chirp induced by the linewidth enhancement factors smears out the TOD effect responsible for the satellites.

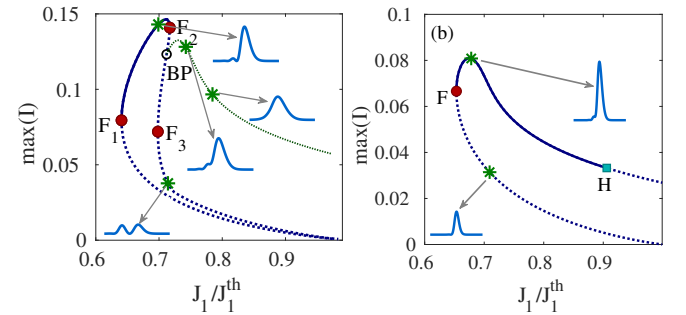


Figure 9. (color online) Branches of the TLSs in the master PDE (28)-(30). The maximum of the field intensity $I = |E|^2$ as a function of the normalized pump current is shown. (a) For $(\alpha_1, \alpha_2) = (0, 0)$ the pulse profiles show defined satellites. The branch has three folds \mathbf{F}_i and a branching point \mathbf{BP} . The second fold \mathbf{F}_2 coincides with an infinite period limit cycle in a global SNIPER bifurcation. An unstable branch emerges from \mathbf{BP} in a pitchfork bifurcation. (b) For $(\alpha_1, \alpha_2) = (1.5, 0.5)$, \mathbf{F}_2 and \mathbf{BP} have merged into an AH bifurcation point \mathbf{H} . The profiles only show intensity bumps on the leading edge of the pulse and there is no longer a SNIPER. Other parameters are $(J_2, \eta, s) = (-0.1, 0.9, 15)$.

Finally, in Fig. 10 we superpose the results on top of data obtained through DNSs of the DAE model (1-4) in the long delay limit using the functional mapping approach [40]. Pulses are fully localized TLSs in this regime. In panel (a) the standard deviation of the pulse energy is shown as a function of the gain bias J_1 normalized to threshold J_1^{th} and the gain linewidth enhancement factor α_1 along with the bifurcation curves from continuation. For small α_1 one can see the satellite unstable region which is similar to the previous parameter set, i.e., close to $\alpha_1 = 0$ there is an additional fold presented in solid blue and the satellite instability sets in as a global SNIPER bifurcation after it. Panel (b) shows a zoom-in on this area where the fold merges with a branching point (dotted blue) thereby forming an AH bifurcation depicted in dash dotted red. Both models quantitatively

agree in this area. The principal fold of the subcritical TLS branch in solid red is also reproduced correctly. For higher α_1 the stable pulse region is limited by another AH bifurcation corresponding to self-phase modulation, shown as well in dash dotted red. In contrast to the DAE, for the PDE model the bifurcation curve slopes down in α_1 for increasing gain. Both the nature of the instability and the discrepancy found in the equivalent PDE are somewhat similar to the bifurcation structure in the Vladimirov-Turaev model for passive mode-locking in a unidirectional ring laser [45, 56].

For the parameters of Fig 10(a) the DAE system exhibits a region close to threshold at high values of α_1 that is partly stable on the high α_1 edge. The corresponding fold and AH curves shown in dotted orange or indicated by red crosses, respectively, are found in the PDE with a qualitatively similar shape but the position of this area is shifted significantly towards lower gain as compared to the DAE. This region corresponds to the bistable region for the previous parameter set. Indeed we found that generally it moves and changes shape significantly as a function of the other parameters and so do the principal pulse and satellite instability regions. For example increasing α_2 makes the stable pulses follow by moving up in α_1 by roughly the same amount, while the satellite instability moves down. The second region moves up in α_1 much quicker and completely detaches, at least when constricting one's view at the area below threshold (see Fig. 11).

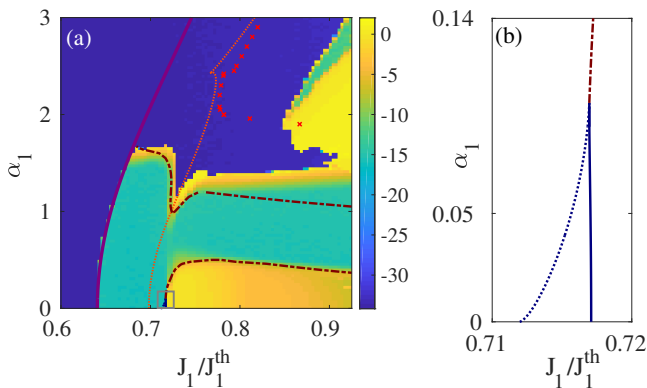


Figure 10. (color online) (a) Bifurcation diagram in the (J_1, α_1) plane of the DAE model (1-4) in the long delay limit superposed with the bifurcation diagram of the equivalent PDE (28)-(30). The color coding shows the standard deviation of the pulse energy obtained by DNSs of the DAE. The evolution of the fold F_1 is marked by a solid red line, the satellite instability around $\alpha_1 = 0$ with the corresponding fold F_3 (branching point) is in solid (dotted) blue and the AH part in dash dotted red. The other AH bifurcation corresponding to self-phase modulation slopes down for the PDE case in contrast to the DAE. The high α_1 region in the PDE is significantly shifted with respect to the DAE. Its fold branch is depicted in dotted orange and AH bifurcations are indicated by red crosses. Parameters are $(J_2, \alpha_2, \eta, s) = (-0.1, 0, 0.9, 15)$. (b) Zoom-in on the SNIPER region where a fold and a branching point merge into an AH bifurcation.

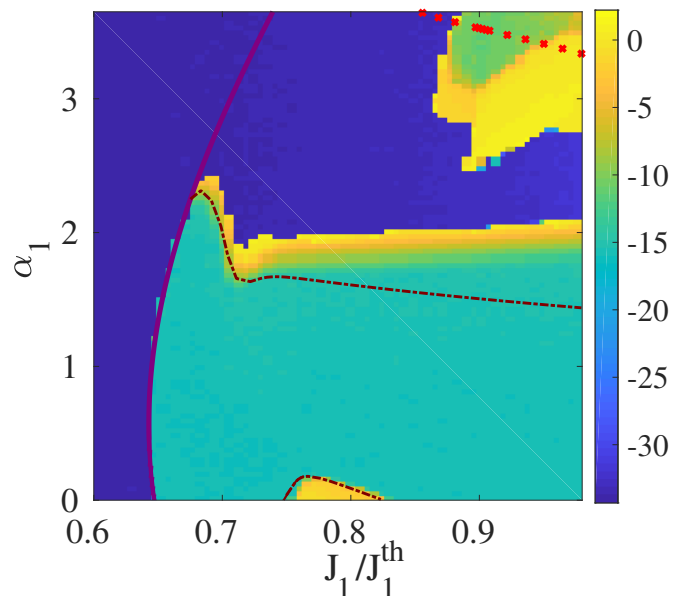


Figure 11. (color online) For larger α_2 the different regions move and deform. The stable pulse region moves up in α_1 by a similar amount while the satellite region moves down. The high α_1 region completely detaches in the area below threshold. Results from bifurcation analysis of the PDE strongly differs from the DAE in this region. Parameters are $(J_2, \alpha_2, \eta, s) = (-0.1, 0.5, 0.9, 15)$.

VII. CONCLUSION

In conclusion, we discussed the dynamics of MIXSELS using a first-principle dynamical model based upon delay algebraic equations. We have found that the third order dispersion induced by the micro-cavity induces satellites on the leading edge of the pulses and shown that the latter can become unstable.

Using a combination of direct time simulations and a path-continuation methods we reconstructed the branch of a single pulse solution. In the limit of vanishing line enhancement factors we show that the onset of the satellite instability is associated with a global bifurcation of the saddle-node infinite period type. The influences of noise as well as features of excitability are discussed.

In the case of non-vanishing linewidth enhancement factors, we showed that the satellite and self-phase modulation instabilities can combine leading to a intricate oscillating dynamics which shed further light on the results obtained in a VCSEL-SESAM setup [22].

Finally, we derived an approximate dispersive master PDE model and performed a full bifurcation analysis. We demonstrated that this PDE reproduces the satellite as well as the low α_1 SNIPER and AH bifurcation structure but it becomes increasingly inaccurate at high α_1 values.

ACKNOWLEDGEMENTS

C.S. and J.J. acknowledge the financial support of the MINECO Project MOVELIGHT (PGC2018-099637-B-I00 AEI/FEDER UE). S.G. acknowledges the PRIME program of the German Academic Exchange Service (DAAD) with funds from the German Federal Ministry of Education and Research (BMBF).

Appendix A: PDE via multiple time scales

We consider in this appendix the derivation of the PDE Eq. 28 by the use of multiple time scale analysis. Our starting point is still Eqs. (A1,A2)

$$\varepsilon \frac{dE}{d\sigma} = [(1 - i\alpha_1) N_1 + (1 - i\alpha_2) N_2 - 1] E + hY \quad (\text{A1})$$

$$Y(\sigma) = \eta [E(\sigma - 1) - Y(\sigma - 1)], \quad (\text{A2})$$

For the sake of simplicity, we set $\alpha_j = 0$ and assume that η is real. It is also convenient for our analysis to transform the system composed of an ODE and a DAE as given by Eqs. (A1,A2) into a single Neutral Differential Delay Equation (NDDE)

$$\varepsilon \left[\frac{dE}{d\sigma}(\sigma) + \eta \frac{dE}{d\sigma}(\sigma - 1) \right] = [(N_1 + N_2) E](\sigma) - E(\sigma) + \eta [(N_1 + N_2) E](\sigma - 1) + (h - 1) \eta E(\sigma - 1), \quad (\text{A3})$$

We can define small deviations of the carriers as

$$N_j = J_j + \varepsilon^3 n_j \quad (\text{A4})$$

with $j \in [1, 2]$ and scale the field, for convenience, as $E = \varepsilon^{\frac{3}{2}} A$. Inserting these scaling relations in Eq. A3, we find

$$A(\sigma) = \eta \frac{h - 1 + N_t}{1 - N_t} A(\sigma - 1) + \frac{\varepsilon^3 \bar{N} - \varepsilon \bar{\mathcal{L}}}{1 - N_t}, \quad (\text{A5})$$

with $N_t = J_1 + J_2$ the threshold inversion given in Eq. 12 and the filtering $\bar{\mathcal{L}}$ and nonlinear operator \bar{N} defined by

$$\bar{\mathcal{L}} = \frac{d}{d\sigma} [A(\sigma) + \eta A(\sigma - 1)] \quad (\text{A6})$$

$$\bar{N} = \sum_{j=1}^{j=2} (n_j A)(\sigma) + \eta (n_j A)(\sigma - 1) \quad (\text{A7})$$

We can now use the definition of threshold given in Eq. 12 to find the system upon which one can perform the multi-scale analysis

$$A(\sigma) = A(\sigma - 1) + \frac{1 + \eta}{h\eta} (\varepsilon^3 \bar{N} - \varepsilon \bar{\mathcal{L}}), \quad (\text{A8})$$

By inspecting Equation A8, one notices that the solutions are weakly perturbed period one (P1) orbits. Because we assume that the nonlinear term scales as ε^3 , we can safely restrict our analysis to the multi-scale analysis on the linear part of Eq. A8, that is

$$A(\sigma) = A(\sigma - 1) - \tilde{\varepsilon} \frac{d}{d\sigma} [A(\sigma) + \eta A(\sigma - 1)], \quad (\text{A9})$$

where we defined the short-hand $\tilde{\varepsilon} = \varepsilon(1 + \eta)/(h\eta)$. The linear NDDE as given by Eq. A9 only depends on

one parameter, which are the cavity losses, and the smallness parameter. It is also an excellent toy model to test various multi-scale schemes. Notice that such a linear NDDE can be solved in the Fourier domain directly. We, however, solve the dynamics by defining a multi-scale expansion. The fast time is $\sigma_0 = \sigma/T$ with T the natural period of the solution. The period T shall be close to unity and its deviation leads to the slow drift in the PDE representation. We set $T = 1 + \tilde{\varepsilon}a$ where a can be chosen to cancel resonant terms in the multi-scale expansion at first order. This approach avoids introducing altogether the intermediate time scale $\sigma_1 = \varepsilon\sigma$. However, one can also find analytically the period of the solution using the functional mapping method which yields $a = 1 + \eta$. Finally, we define the slow times $\sigma_2 = \tilde{\varepsilon}^2\sigma$ and $\sigma_3 = \tilde{\varepsilon}^3\sigma$ in order to take into account the effect of nonlinearity, diffusion and third order dispersion. The chain rule yields

$$\frac{d}{d\sigma} \rightarrow \frac{1}{T} \frac{\partial}{\partial \sigma_0} + \tilde{\varepsilon}^2 \frac{\partial}{\partial \sigma_2} + \tilde{\varepsilon}^3 \frac{\partial}{\partial \sigma_3} \quad (\text{A10})$$

while for the conjugated Fourier variables, we have

$$\omega_\sigma \rightarrow \frac{1}{T} \omega_0 + \tilde{\varepsilon}^2 \omega_2 + \tilde{\varepsilon}^3 \omega_3 \quad (\text{A11})$$

We expand the solution as

$$A(\sigma_0, \sigma_2, \sigma_3) = \sum_{j=0}^{\infty} \varepsilon^j A_j(\sigma_0, \sigma_2, \sigma_3) \quad (\text{A12})$$

The various solvability conditions lead to several conditions of the form $\bar{L}\hat{A}(\omega_0, \omega_2, \omega_3) = 0$ where $\hat{A}(\omega_0, \omega_2, \omega_3)$ is the (triple) Fourier transform of $A(\sigma_0, \sigma_2, \sigma_3)$. The expression of \bar{L} is

$$\bar{L}(\omega_\sigma) = \exp(i\omega_\sigma) - 1 + i\tilde{\varepsilon}\omega_\sigma [1 + \eta \exp(i\omega_\sigma)] \quad (\text{A13})$$

The zeroth order operator reads naturally

$$\bar{L}_0 = e^{i\omega_0} - 1 \quad (\text{A14})$$

hence showing that P1 solutions on the fast scale σ_0 , i.e. $A_0(\sigma_0 - 1, \sigma_2, \sigma_3) = A_0(\sigma_0, \sigma_2, \sigma_3)$, belong to the kernel of \bar{L}_0 . The first order solvability is trivially solved since $\bar{L}_1 = 0$ due to our adequate choice of the period T . The other operators found at second and third order are more complex, yet they simplify when acting on P1 solutions,

$$\bar{L}_2 = (\eta^2 - 1)\omega_0^2 + 2i\omega_2, \quad (\text{A15})$$

$$\bar{L}_3 = -i\frac{\eta^3 + 1}{3}\omega_0^3 - \frac{\eta - 1}{2}(\eta + 1)^2\omega_0^2 + i\omega_3. \quad (\text{A16})$$

One can then build the conjugated variable to the slow time ω_ξ as

$$\omega_\xi = \left(\frac{1}{T} - 1\right)\omega_0 + \omega_2\tilde{\varepsilon}^2 + \omega_3\tilde{\varepsilon}^3$$

We note that adding the $-\omega_0$ corresponds to the stroboscopic effect that transforms a T -periodic solution into a slowly drifting steady state from one round-trip to the

other. Upon simplification, we find

$$-i\omega_\xi = i(1 + \eta)\tilde{\omega} + \frac{\eta^2 - 1}{2}\tilde{\omega}^2 - i\frac{\eta^3 + 1}{3}\tilde{\omega}^3 + \mathcal{O}(\varepsilon)$$

where we defined $\tilde{\varepsilon}\omega_0 = \tilde{\omega}$. Using the definition of $\tilde{\varepsilon}$ and going back to the original variable, i.e. $\varepsilon\omega_0 \rightarrow \omega$, gives the following expression for the slow evolution

$$\omega_\xi = d_1\omega - id_2\omega^2 - d_3\omega^3 \quad (\text{A17})$$

with the coefficients d_j defined in Eq. 28. Finally, using that $-i\omega \rightarrow \partial_z$ we get

$$\partial_\xi = d_1\partial_z + d_2\partial_z^2 + d_3\partial_z^3 \quad (\text{A18})$$

As we assumed that the nonlinear term scales as ε^3 , it can simply be added to the highest order solvability condition found for the operator \bar{L}_3 . By using that the carriers are also P1 solutions on the fast time scale (σ_0) we get that $(n_j A)(\sigma_0 - 1, \sigma_2, \sigma_3) = (n_j A)(\sigma_0, \sigma_2, \sigma_3)$ with $j \in [1, 2]$ which allows finding the PDE in the main manuscript.

-
- [1] Hans W. Mocker and R. J. Collins. Mode competition and self-locking effects in a Q -switched ruby laser. *Applied Physics Letters*, 7(10):270–273, 1965. **I**
- [2] D. Lorenser, H. J. Unold, D. J. H. C. Maas, A. Aschwanden, R. Grange, R. Paschotta, D. Ebling, E. Gini, and U. Keller. Towards wafer-scale integration of high repetition rate passively mode-locked surface-emitting semiconductor lasers. *Appl. Phys. B*, 79:927–932, 2004. **I**
- [3] U. Keller, K. J. Weingarten, F. X. Kärtner, D. Kopf, B. Braun, I. D. Jung, R. Fluck, C. Hönninger, N. Matuschek, and J. Aus der Au. Semiconductor saturable absorber mirrors (SESAM's) for femtosecond to nanosecond pulse generation in solid-state lasers. *Selected Topics in Quantum Electronics, IEEE Journal of*, 2:435–453, 1996. **I**
- [4] A. Gordon and B. Fischer. Phase transition theory of many-mode ordering and pulse formation in lasers. *Physical Review Letters*, 89:103901–3, 2002. **I**
- [5] R. Weill, A. Rosen, A. Gordon, O. Gat, and B. Fischer. Critical behavior of light in mode-locked lasers. *Physical Review Letters*, 95:013903, 2005. **I**
- [6] Arnaud Garnache, Vincent Lecocq, Laurence Ferrières, Attia Benselama, Mikhaël Myara, Laurent Cerutti, Isabelle Sagnes, and Stéphane Denet. Industrial integration of high coherence tunable vcsel in the nir and mir. *Proc.SPIE*, 8966:8966 – 8966 – 10, 2014. **I**
- [7] M. Devautour, A. Michon, G. Beaudoin, I. Sagnes, L. Cerutti, and A. Garnache. Thermal management for high-power single-frequency tunable diode-pumped vcsel emitting in the near- and mid-ir. *IEEE Journal of Selected Topics in Quantum Electronics*, 19(4):1701108–1701108, July 2013.
- [8] N. Takeuchi, N. Sugimoto, H. Baba, and K. Sakurai. Random modulation cw lidar. *Appl. Opt.*, 22(9):1382–1386, May 1983.
- [9] Nobuo Takeuchi, Hiroshi Baba, Katsumi Sakurai, and Toshiyuki Ueno. Diode-laser random-modulation cw lidar. *Applied Optics*, 25:63–67, 1985. **I**
- [10] H. A. Haus. Mode-locking of lasers. *IEEE J. Selected Topics Quantum Electron.*, 6:1173–1185, 2000. **I, VI**
- [11] E. Avrutin and J. Javaloyes. *Mode-Locked Semiconductor Lasers, Book Chapter In: Handbook of Optoelectronic Device Modeling and Simulation*. CRC press, Taylor and Francis, United Kingdom, 2017. **I**
- [12] S. M. Link, D. J. H. C. Maas, D. Waldburger, and U. Keller. Dual-comb spectroscopy of water vapor with a free-running semiconductor disk laser. *Science*, 356(6343):1164–1168, 2017. **I**
- [13] Th Udem, R. Holzwarth, and T. W. Hänsch. Optical frequency metrology. *Nature*, 416(6877):233–237, 2002. **I**
- [14] S. Hoogland, S. Dhanjal, A. C. Tropper, J. S. Roberts, R. Häring, R. Paschotta, F. Morier-Genoud, and U. Keller. Passively mode-locked diode-pumped surface-emitting semiconductor lasers. *IEEE Photonics Technology Letters*, 12:1135–1137, 2000. **I**
- [15] R. Häring, R. Paschotta, E. Gini, F. Morier-Genoud, D. Martin, H. Melchior, and U. Keller. Picosecond surface-emitting semiconductor laser with > 200 mw average power. *Electronics Letters*, 37(12):766–767, Jun 2001.
- [16] R. Häring, R. Paschotta, A. Aschwanden, E. Gini, F. Morier-Genoud, and U. Keller. High-power passively mode-locked semiconductor lasers. *Quantum Electronics, IEEE Journal of*, 38:1268–1275, 2002. **I**
- [17] B. Rudin, A. Rutz, M. Hoffmann, D. J. H. C. Maas, A.-R. Bellancourt, E. Gini, T. Südmeyer, and U. Keller. Highly efficient optically pumped vertical-emitting semiconductor laser with more than 20 w average output power in

- a fundamental transverse mode. *Opt. Lett.*, 33(22):2719–2721, Nov 2008. **I**
- [18] Dominik Waldburger, Sandro M. Link, Mario Mangold, Cesare G. E. Alfieri, Emilio Gini, Matthias Golling, Bauke W. Tilma, and Ursula Keller. High-power 100 fs semiconductor disk lasers. *Optica*, 3(8):844–852, Aug 2016. **I**
- [19] D.J.H.C. Maas, A.-R. Bellancourt, B. Rudin, M. Golling, H.J. Unold, T. Südmeyer, and U. Keller. Vertical integration of ultrafast semiconductor lasers. *Applied Physics B*, 88(4):493–497, Sep 2007. **I**
- [20] B. Rudin, V. J. Wittwer, D. J. H. C. Maas, M. Hoffmann, O. D. Sieber, Y. Barbarin, M. Golling, T. Südmeyer, and U. Keller. High-power mixsel: an integrated ultrafast semiconductor laser with 6.4 w average power. *Opt. Express*, 18(26):27582–27588, Dec 2010. **I**
- [21] P. Camelin, C. Schelte, A. Verschelde, A. Garnache, G. Beaudoin, I. Sagnes, G. Huyet, J. Javaloyes, S. V. Gurevich, and M. Giudici. Temporal localized structures in mode-locked vertical external-cavity surface-emitting lasers. *Opt. Lett.*, 43(21):5367–5370, Nov 2018. **I**
- [22] C. Schelte, P. Camelin, M. Marconi, A. Garnache, G. Huyet, G. Beaudoin, I. Sagnes, M. Giudici, J. Javaloyes, and S. V. Gurevich. Third order dispersion in time-delayed systems. *Phys. Rev. Lett.*, 123:043902, Jul 2019. **I, II, III, V, VII**
- [23] Lina Jaurigue, Oleg Nikiforov, Eckehard Schöll, Stefan Breuer, and Kathy Lüdge. Dynamics of a passively mode-locked semiconductor laser subject to dual-cavity optical feedback. *Phys. Rev. E*, 93:022205, Feb 2016. **I**
- [24] Lina Jaurigue, Bernd Krauskopf, and Kathy Lüdge. Multiple pulse dynamics of a passively mode-locked semiconductor laser with delayed optical feedback. *Chaos: An Interdisciplinary Journal of Nonlinear Science*, 27(11):114301, 2017. **I**
- [25] R. M. Arhipov, T. Habruseva, A. Pimenov, M. Radziunas, S. P. Hegarty, G. Huyet, and A. G. Vladimirov. Semiconductor mode-locked lasers with coherent dual-mode optical injection: simulations, analysis, and experiment. *J. Opt. Soc. Am. B*, 33(3):351–359, Mar 2016. **I**
- [26] Yifan Sun Sun, Sylvain Combrié, Fabien Bretenaker, and Alfredo De Rossi. Mode locking of the hermite-gaussian modes of a nanolaser. *Phys. Rev. Lett.*, in print, 2019. **I**
- [27] M. Rossetti, P. Bardella, and I. Montrosset. Modeling passive mode-locking in quantum dot lasers: A comparison between a finite-difference traveling-wave model and a delayed differential equation approach. *Quantum Electronics, IEEE Journal of*, 47(5):569–576, may 2011. **I**
- [28] Stefan Breuer, Dimitris Syvridis, and Edik U. Rafailov. *Ultra-Short-Pulse QD Edge-Emitting Lasers*, pages 43–94. Wiley-VCH Verlag GmbH & Co. KGaA, 2014. **I**
- [29] C. G. E. Alfieri, D. Waldburger, J. Nürnberg, M. Golling, L. Jaurigue, K. Lüdge, and U. Keller. Mode-locking instabilities for high-gain semiconductor disk lasers based on active submonolayer quantum dots. *Phys. Rev. Applied*, 10:044015, Oct 2018. **I**
- [30] T. Malica, J. Lin, T. Ackemann, D. J. Little, J. P. Toomey, D. Paboeuf, W. Lubeigt, N. Hempler, G. Malcolm, G. T. Maker, and D. M. Kane. Mapping the dynamical regimes of a sesam mode-locked vecsel with a long cavity using time series analysis. *Opt. Express*, 26(13):16624–16638, Jun 2018. **I**
- [31] Jan Hausen, Stefan Meinecke, Benjamin Lingnau, and Kathy Lüdge. Pulse cluster dynamics in passively mode-locked semiconductor vertical-external-cavity surface-emitting lasers. *Phys. Rev. Applied*, 11:044055, Apr 2019. **I**
- [32] M. Marconi, J. Javaloyes, S. Balle, and M. Giudici. How lasing localized structures evolve out of passive mode locking. *Phys. Rev. Lett.*, 112:223901, Jun 2014. **I, III**
- [33] P. Camelin, J. Javaloyes, M. Marconi, and M. Giudici. Electrical addressing and temporal tweezing of localized pulses in passively-mode-locked semiconductor lasers. *Phys. Rev. A*, 94:063854, Dec 2016.
- [34] J. Javaloyes, P. Camelin, M. Marconi, and M. Giudici. Dynamics of localized structures in systems with broken parity symmetry. *Phys. Rev. Lett.*, 116:133901, Mar 2016.
- [35] Serhiy Yanchuk, Stefan Ruschel, Jan Sieber, and Matthias Wolfrum. Temporal dissipative solitons in time-delay feedback systems. *Phys. Rev. Lett.*, 123:053901, Jul 2019. **I**
- [36] Albert Schliesser, Nathalie Picqué, and Theodor W. Hänsch. Mid-infrared frequency combs. *Nature Photonics*, 6(7):440–449, 2012. **I**
- [37] Ursula Keller. Recent developments in compact ultrafast lasers. *Nature*, 424(6950):831–838, 2003. **I**
- [38] J. Javaloyes. Cavity light bullets in passively mode-locked semiconductor lasers. *Phys. Rev. Lett.*, 116:043901, Jan 2016. **I**
- [39] S. V. Gurevich and J. Javaloyes. Spatial instabilities of light bullets in passively-mode-locked lasers. *Phys. Rev. A*, 96:023821, Aug 2017.
- [40] C. Schelte, J. Javaloyes, and S. V. Gurevich. Functional mapping for passively mode-locked semiconductor lasers. *Opt. Lett.*, 43(11):2535–2538, Jun 2018. **I, IV, VI**
- [41] F. Gires and P. Tournois. Interferometre utilisable pour la compression d’impulsions lumineuses modulees en frequence. *C. R. Acad. Sci. Paris*, (258):6112–6115, 1964. **I, II**
- [42] J. Mulet and S. Balle. Mode locking dynamics in electrically-driven vertical-external-cavity surface-emitting lasers. *Quantum Electronics, IEEE Journal of*, 41(9):1148–1156, 2005. **I, II**
- [43] Ali H Nayfeh. *The Method of Normal Forms*. John Wiley & Sons, Hoboken, NJ, 2011. **I**
- [44] Hannes Uecker, Daniel Wetzels, and Jens D. M. Rademacher. pde2path - a matlab package for continuation and bifurcation in 2d elliptic systems. *Numerical Mathematics: Theory, Methods and Applications*, 7(1):58–106, 002 2014. **I, VI**
- [45] A. G. Vladimirov and D. Turaev. Model for passive mode locking in semiconductor lasers. *Phys. Rev. A*, 72:033808, Sep 2005. **II, III, VI, VI**
- [46] G. Giacomelli and A. Politi. Relationship between delayed and spatially extended dynamical systems. *Phys. Rev. Lett.*, 76:2686–2689, Apr 1996. **II**
- [47] S.A. Kashchenko. The Ginzburg-Landau equation as a normal form for a second-order difference-differential equation with a large delay. *Comput. Math. Math. Phys.*, 38(3):1, 1998. **II**
- [48] Giovanni Giacomelli, Francesco Marino, Michael A. Zaks, and Serhiy Yanchuk. Nucleation in bistable dynamical systems with long delay. *Phys. Rev. E*, 88:062920, Dec 2013. **II**
- [49] Laurent Larger, Bogdan Penkovsky, and Yuri Maistrenko. Virtual chimera states for delayed-feedback

- systems. *Phys. Rev. Lett.*, 111:054103, Aug 2013.
- [50] Francesco Marino, Giovanni Giacomelli, and Stephane Barland. Front pinning and localized states analogues in long-delayed bistable systems. *Phys. Rev. Lett.*, 112:103901, Mar 2014.
- [51] Serhiy Yanchuk and Giovanni Giacomelli. Pattern formation in systems with multiple delayed feedbacks. *Phys. Rev. Lett.*, 112:174103, May 2014.
- [52] Thomas Erneux, Julien Javaloyes, Matthias Wolfrum, and Serhiy Yanchuk. Introduction to focus issue: Time-delay dynamics. *Chaos: An Interdisciplinary Journal of Nonlinear Science*, 27(11):114201, 2017. [II](#), [VI](#)
- [53] Serhiy Yanchuk and Giovanni Giacomelli. Spatio-temporal phenomena in complex systems with time delays. *Journal of Physics A: Mathematical and Theoretical*, 50(10):103001, 2017. [II](#), [VI](#)
- [54] R. Lang and K. Kobayashi. External optical feedback effects on semiconductor injection laser properties. *Quantum Electronics, IEEE Journal of*, 16(3):347 – 355, mar 1980. [II](#)
- [55] K. Engelborghs, T. Luzyanina, and D. Roose. Numerical bifurcation analysis of delay differential equations using dde-biftool. *ACM Trans. Math. Softw.*, 28(1):1–21, March 2002. [III](#)
- [56] C. Schelte, J. Javaloyes, and S. V. Gurevich. Dynamics of temporally localized states in passively mode-locked semiconductor lasers. *Phys. Rev. A*, 97:053820, May 2018. [III](#), [VI](#)
- [57] Theodore Kolokolnikov, Michel Nizette, Thomas Erneux, Nicolas Joly, and Serge Bielawski. The Q -switching instability in passively mode-locked lasers. *Physica D: Nonlinear Phenomena*, 219(1):13 – 21, 2006. [VI](#)